International Journal of Heat and Technology
Vol. 44, No. 3, June, 2026, pp. 1017-1033
Journal homepage: http://iieta.org/journals/ijht

AI-Driven Thermal-Hydraulic Optimization of a Serpentine Water–Air Heat Exchanger Using Computational Fluid Dynamics Analysis

Feras N. Hasoon[1], Abadal-Salam T. Hussain[2], Tareq Hamad Abed[3], Nurettin Gökşenli[4], Abdulhassan Abed Karamallah[5], Enes Bektaş[6], Taha Almulaisi[7*]

[1] Department of Electrical and Communication Engineering, National University of Science & Technology, Muscat 112, Oman
[2] Department of Medical Instrumentation Techniques Engineering, Technical Engineering College, Al-Kitab University, Altun Kupri, Kirkuk 36001, Iraq
[3] Renewable Energy Research Centre, University of Anbar, Anbar 31001, Iraq
[4] Department of Electronics and Automation, Çankırı Karatekin University, Çankırı 18100, Türkiye
[5] Department of Power Mechanics Engineering Techniques, Technical College of Engineering, Al-Bayan University, Baghdad 10011, Iraq
[6] Department of Electrical and Electronics Engineering, Çankırı Karatekin University, Çankırı 18100, Türkiye
[7] Renewable Energy Research Unit, Polytechnic College Hawija, Northern Technical University, Hawija 36007, Iraq

Corresponding Author Email: taha.a.taha@ntu.edu.iq

https://doi.org/10.18280/ijht.440311

Received: 5 April 2026
Revised: 9 June 2026
Accepted: 22 June 2026
Available online: 30 June 2026

Keywords:
Computational Fluid Dynamics, Dean-vortex enhancement, NSGA-II multi-objective optimization, serpentine heat exchanger, machine-learning surrogate model

ABSTRACT

Serpentine water–air heat exchangers play a central role in heating, ventilation, and air-conditioning (HVAC) equipment, automotive radiators, fuel-cell humidifiers, photovoltaic-thermal collectors, and the cold-plate cooling of high-power electronics; yet their high-dimensional design space—spanning hydraulic diameter, bend curvature, pass count, fin geometry, and dual-stream flow rates- defies conventional trial-and-error tuning. This study introduces a reproducible Artificial Intelligence-Computational Fluid Dynamics (AI-CFD) pipeline that integrates four elements into an end-to-end framework: a Dean-corrected validated CFD-correlation engine; a head-to-head benchmark of three surrogate families on five thermal-hydraulic targets; a Non-dominated Sorting Genetic Algorithm II (NSGA-II) Pareto search; and a Technique for Order of Preference by Similarity to Ideal Solution (TOPSIS) compromise rule that returns an engineering-realistic optimum rather than a mathematical extremum. Six hundred Latin-Hypercube design points feed the surrogates. The best surrogate (a 64-64-32 multilayer Artificial Neural Network (ANN)) reaches $R^2 = 0.989$ for heat duty, 0.979 for effectiveness, and 0.987 for the Performance Evaluation Criterion (PEC), with mean absolute percentage errors below 4% for these three targets. Compared with a representative industrial baseline, the AI-selected design simultaneously raises duty by 31.2%, lifts effectiveness from 0.37 to 0.77 (≈ +108%), trims water-side and air-side pressure drops by 70.7% and 82.9%, and reduces total pumping power by 88.0%, yielding a PEC of 5.94. Sensitivity analysis reveals that the pass count, water mass-flow rate, and fin height are the dominant parameters for heat duty and effectiveness, whereas the bend radius and fin height govern the PEC through the balance between Dean-vortex enhancement and the associated friction penalty. The pipeline takes less than 90 s to complete on a workstation, which is over two orders of magnitude faster than similar direct-CFD optimization pipelines.

1. INTRODUCTION

The serpentine heat exchanger topology, which features a single bent tube, is poised at the intersection of energy efficiency, electrification, and thermal management. They are found in the vehicle radiator, fuel-cell humidification loops, photovoltaic-thermal collectors, district heating substations, and, more and more, in the cold-plate cooling of Graphics Processing Units (GPUs) and lithium-ion battery packs. The serpentine arrangement (made up of a single tube that snakes through a finned air channel) has a large amount of heat-transfer area in a small volume, naturally produces secondary Dean-vortex flow at each U-bend, and does not have any of the header-distribution issues inherent in parallel-tube systems [1, 2]. The very same curvature that raises the local Nusselt number simultaneously raises friction, and the resulting trade-off is highly non-linear in geometry and operating conditions.

Recent computational and experimental work has tracked three intersecting threads. The first concerns advanced turbulence and conjugate modelling in curved channels [3, 4]. The second focuses on passive intensification through fins, dimples, twisted tapes, surface pits and phase-change media [5-7]. The third — and most rapidly evolving — replaces expensive direct Computational Fluid Dynamics (CFD) with data-driven surrogates and artificial intelligence (AI)-assisted search [8-10]. Within this third stream, Alharbi et al. [11] applied a Cattaneo–Christov (non-Fourier) heat-flux model to three-dimensional nanofluid flow and showed that thermal-relaxation effects measurably alter the effective Nusselt number. Aghaei et al. [12] simulated turbulent transport in sinusoidal pulsating offset jets and showed a strong dependence of the local Nu profile on Strouhal number — a result that maps directly onto the unsteady crossflow encountered between adjacent serpentine passes. Shakir et al. [13] developed an iterative correlation scheme for the air heat flow over finned tubes and validated it against several published correlations, providing a useful baseline for the air-side resistance term used here. Sobale et al. [14] examined the stagnation flow of a Williamson nanofluid with porosity, chemical reaction and internal heating, underscoring non-Newtonian rheology as an emerging enhancement lever. At the system level, Munimathan et al. [15] experimentally analyzed a two-stage scroll compressor operating with R32 refrigerant, with and without vapour injection, in a heat pump, quantifying the effect of vapour injection on heating capacity and coefficient of performance. Yosif and Mustaffa Saleem [16] experimentally compared lauric acid and paraffin wax as latent storage media in a single-pass solar air heater; Alrefaee et al. [17] quantified the influence of surface pits on a double-tube heat exchanger; and Haider et al. [18] evaluated an oscillating heat-sink geometry under free convection. These studies [11-18] together map the contemporary frontier of passive and active enhancement that frames the present study.

Migration toward physics-aware and surrogate-based design has accelerated noticeably in recent years. Yang et al. [19] combined global sensitivity analysis with the Non-dominated Sorting Genetic Algorithm II (NSGA-II) to optimize the thermal design of plate-fin heat exchangers. Huang et al. [20] benchmarked Artificial Neural Networks (ANNs), support-vector machines, random forests and Gaussian-process regression for microchannel heat exchangers and obtained the highest accuracy with the Gaussian-process and neural-network models. Li et al. [21] applied machine-learning methods to the thermal-hydraulic performance of printed-circuit heat exchangers operating with supercritical methane. Across these studies [22-28], surrogate-driven workflows now consistently report 50-400× speed-ups relative to direct-CFD design loops. However, a common drawback is methodology: most studies optimize one objective (only Q, only ε, or only ΔP), and this Pareto trade-off between the two is not exposed. The effect of secondary flow induced by curvature is well known to be a Nusselt-enhancement scaling as $De^{0.6}\mathrm{Pr}^{0.25}$ in the laminar-transitional flow regime, where $De = Re \cdot \left(\frac{D_t}{2R_b}\right)^{0.5}$ and the flow is defined as being laminar at $R_e < 10{,}000$ and fully turbulent at $R_e > 10{,}000$. The secondary flow due to curvature has been studied extensively and more recently is found to be Nusselt-enhanced in the laminar-transitional flow regime as $De^{0.6}\mathrm{Pr}^{0.25}$ with $De = Re \cdot \left(\frac{D_t}{2R_b}\right)^{0.5}$, and the effect weakens as the flow becomes fully turbulent, $R_e > 10{,}000$, with reassessment [29, 30] that the Nusselt-weakening effect is not observed. On the air side, recent reviews [31, 32] have identified fin pitch and fin height as the two most powerful geometric levers and fin efficiency as a multiplicative factor of the external surface available [33-35].

Three gaps persist in the current literature, despite its rapid expansion. First, very few studies present a fully reproducible, end-to-end pipeline that flows continuously from geometric parameterization through Pareto selection without manual intervention. Second, the simultaneous treatment of thermodynamic targets (Q, ε, U) and hydraulic targets $(\Delta P_w, \Delta P_a, P_{pump})$, bound together by a single Performance Evaluation Criterion (PEC), is rarely reported on the same data. Third, almost every published Artificial Intelligence-Computational Fluid Dynamics (AI-CFD) framework relies on a single learner, leaving the comparative reliability of Random Forest, gradient-boosted ensembles and deep neural networks for thermal-hydraulic regression an open question [36-46].

The contribution of the present work, which directly addresses these three gaps, is four-fold and is summarized here so that the novelty is unambiguous:

•A fully reproducible AI-CFD pipeline is built around a 600-point Latin Hypercube Sampling (LHS) design-of-experiments (DOE) fed to a Dean-corrected correlation engine that is independently validated against the Gnielinski equation to within 3.4% mean error.

•Three surrogate families — Random Forest, Gradient-Boosting Regressor and a multi-layer ANN-are benchmarked head-to-head on five simultaneous targets $(Q, \Delta P_w, \Delta P_a, \varepsilon, PEC)$. To our knowledge, this is the first such head-to-head benchmark on a serpentine geometry under a unified DOE.

•NSGA-II is paired with a Technique for Order of Preference by Similarity to Ideal Solution (TOPSIS) compromise rule (weighting vector w = [0.40, 0.25, 0.20, 0.15] over Q, P_{pump}, ε, PEC), so that the returned design lies at the engineering-useful knee of the Pareto front rather than at a mathematical extremum that ignores cost or manufacturability.

•The selected optimum is verified by re-running the full thermal-hydraulic model and is benchmarked against an industry-typical baseline, providing a transparent quantification of the engineering value (+31.2% duty, +108% effectiveness, −88.0% pumping power) that single-objective approaches in studies [19, 21] cannot deliver.

Followingly, this is therefore tangible in comparison to other similar optimization schemes, like hybrid or surrogate heat-exchanger optimization. Previous research [19, 20] has been based on one learner and one objective; in this research three learners and five targets are used. The optimization is done in the latent space [21, 26] without checking the optimum with the underlying CFD model, while our optimization is verified by back-substitution, and the difference compared to baseline is reported. TOPSIS with transparently documented weights is attached, whereas studies [22, 24] present only Pareto fronts without an explicit compromise rule, which can be reproduced through the recommended design. The rest of the paper is structured according to the common fashion; in Section 2 the geometry is described and the governing equations are presented following by the validation and AI workflow; in Section 3 multi-objective optimization basis are presented, in Section 4 the results are reported, compared with recent state of the art and discussed on the physical interpretation; in Section 5 a limitations-aware future-work plan is proposed, and finally conclusion is presented in Section 6.

2. METHODOLOGY

2.1 Physical configuration and geometric parameterization

The copper tube in the studied unit is circular and wound through a single straight pass horizontally with 180° U-bends of mean radius R_b. Aluminium plate-fins are bonded to the outside of the tubes to improve the coefficient on the air-side. The schematic is depicted in Figure 1 with the water inlet and outlet, the cross-flow air stream and the finned channel. Six geometric variables and two operating mass-flow rates are treated as design variables (Table 1), with bounds chosen to span the practical envelope of heating, ventilation, and air-conditioning (HVAC)- and automotive-class radiators: tube inner diameter $D_t \in [8, 20]$ mm, bend radius $R_b \in [20, 60]$ mm, number of passes $n_p \in [4, 12]$, pass length $L_p \in [0.20, 0.60]$ m, fin pitch $p_f \in [2.0, 6.0]$ mm, fin height $h_f \in [5, 20]$ mm, water mass flow $\dot{m}_w \in [0.09, 0.36] kg\ s^{-1}$, and air mass flow $\dot{m}_a \in [0.22, 1.10] kg\ s^{-1}$. The inlet temperatures are set to $T_w, in = 60$ ℃ and $T_a, in = 25$ ℃, which closely match the engine-cooling duty cycle and HVAC duty cycle, respectively. The complete computational workflow, from geometric parameterization through LHS and surrogate training to the final compromise selection, is summarized in Figure 2.

2.2 Governing equations

The thermohydraulic model couples conservation of mass, momentum and energy with validated heat-transfer and friction correlations. Eqs. (1)-(3) state continuity, momentum and energy at the cell level:

$$\frac{\partial \rho}{\partial t} + \nabla \cdot (\rho u) = 0 \tag{1}$$

$$\frac{\partial (\rho u)}{\partial t} + \nabla \cdot (\rho u u) = -\nabla p + \nabla \cdot \tau + \rho g \tag{2}$$

$$\frac{\partial (\rho c p T)}{\partial t} + \nabla \cdot (\rho c p u T) = \nabla \cdot (k \nabla T) + \Phi \tag{3}$$

where, τ the viscous-stress tensor and Φ the viscous-dissipation term. The water-side friction factor in smooth straight tubes follows the Hagen-Poiseuille relation in Eq. (4) for laminar flow and the Petukhov form in Eq. (5) for turbulent flow:

$$f_{lam} = \frac{64}{Re} \tag{4}$$

$$f_{turb} = (0.790 \cdot \log(Re) - 1.64)^{-2} \tag{5}$$

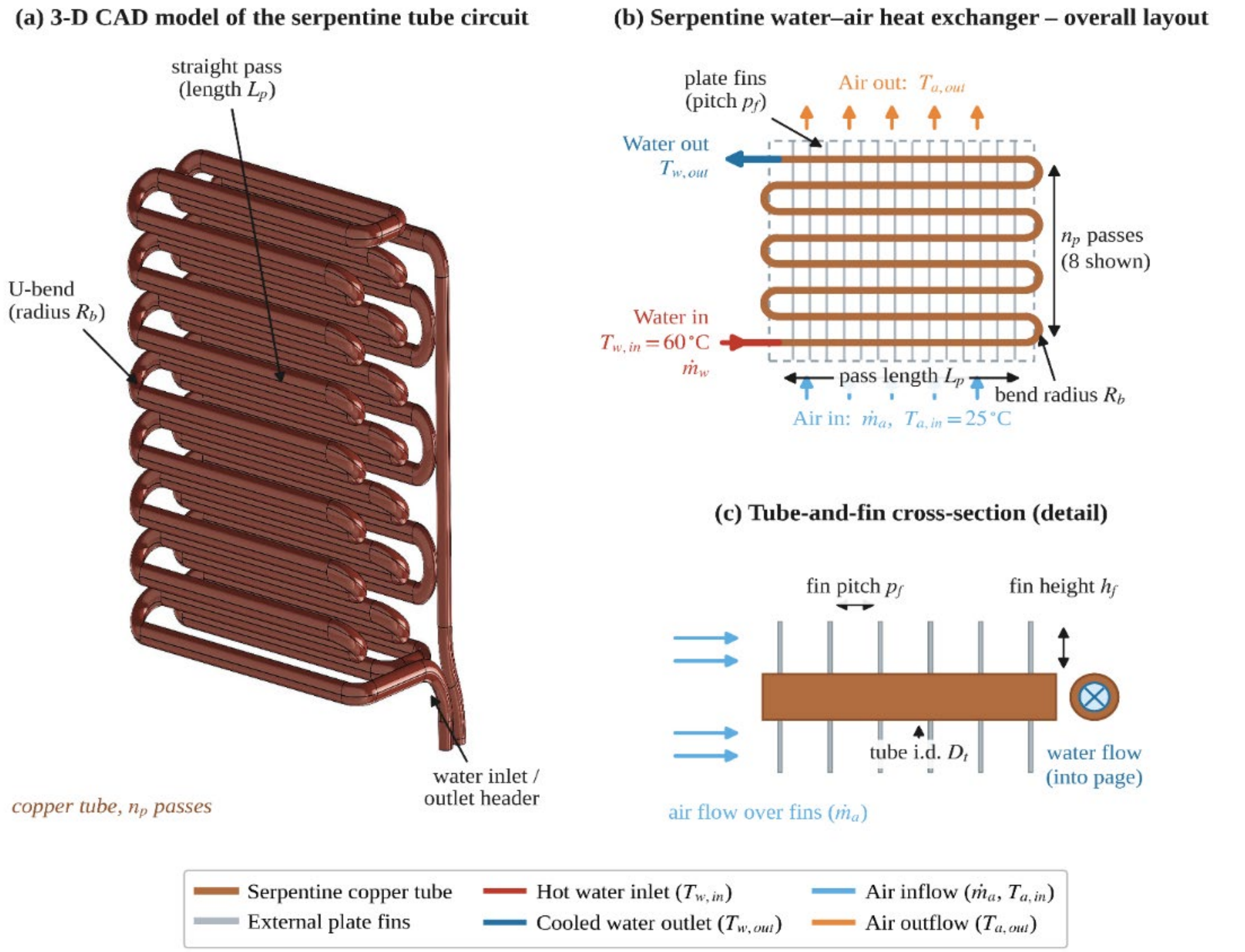

Figure 1. Serpentine water–air heat exchanger: (a) 3-D CAD model; (b) overall layout with design variables; (c) tube-and-fin cross-section

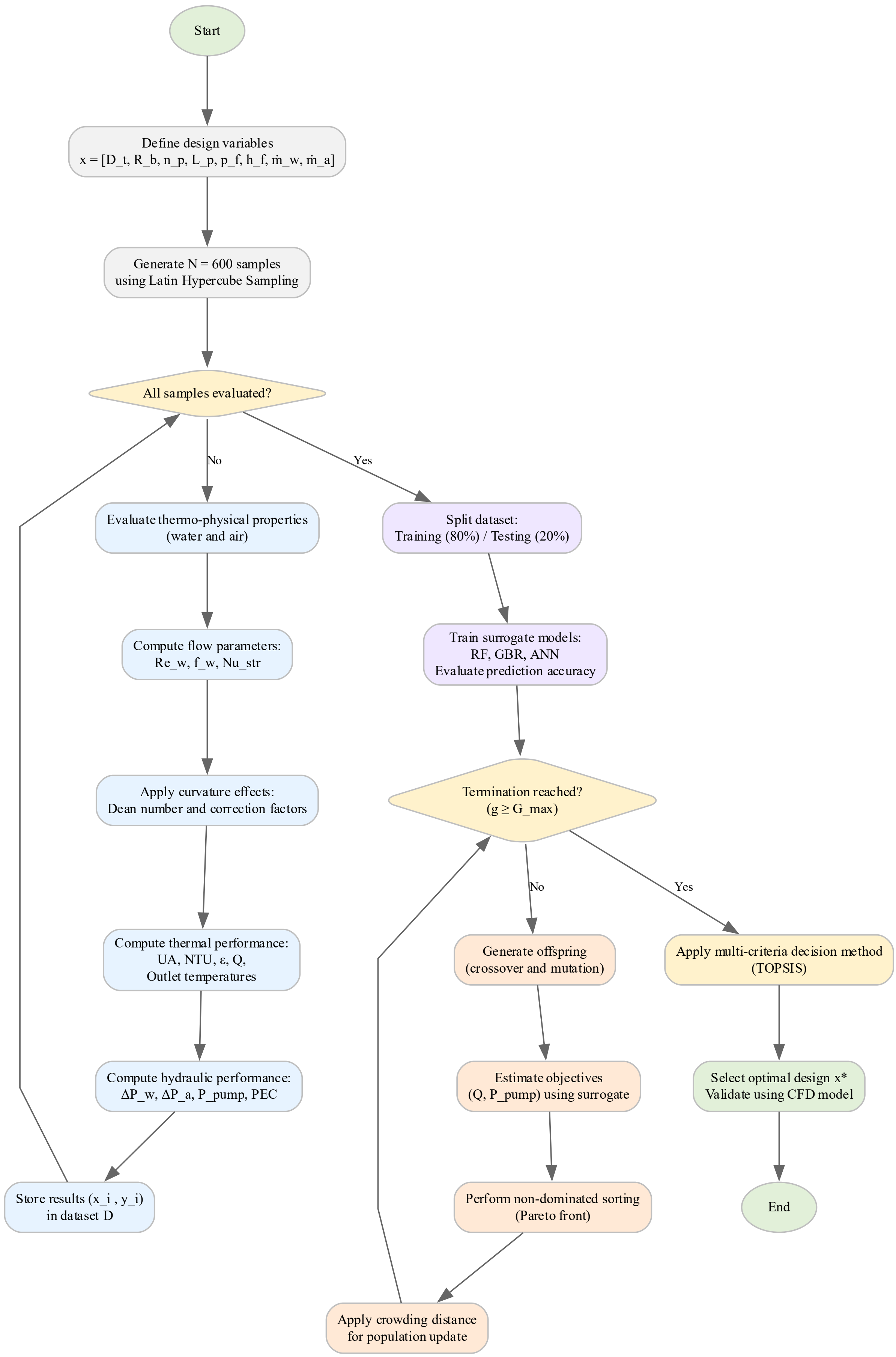

Figure 2. End-to-end AI-CFD workflow: parameterization, Latin-Hypercube DOE, validated correlation engine, surrogate training, NSGA-II Pareto search, and TOPSIS compromise selection

Note: AI-CFD: Artificial Intelligence-Computational Fluid Dynamics; DOE: Design of Experiments; LHS: Latin Hypercube Sampling; RF: Random Forest; GBR: Gradient Boosting Regressor; ANN: Artificial Neural Network; NSGA-II: Non-dominated Sorting Genetic Algorithm II.

Table 1. Design variables and their ranges, fixed operating conditions, and property-evaluation basis

Parameter	Symbol	Range / Value	Unit
Design variables (Latin-Hypercube-sampled)			
Tube inner diameter	D_t	8-20	mm
Bend radius	R_b	20-60	mm
Number of passes	n_p	4-12	-
Pass length	L_p	0.20-0.60	m
Fin pitch	p_f	2.0-6.0	mm
Fin height	h_f	5-20	mm
Water mass-flow rate	$\dot{m}_w$	0.09-0.36	kg s⁻¹
Air mass-flow rate	$\dot{m}_a$	0.22-1.10	kg s⁻¹
Fixed operating conditions			
Water inlet temperature	$T_{w,in}$	60	°C
Air inlet temperature	$T_{a,in}$	25	°C
Fixed model parameters and property basis			
Tube material	—	Copper	—
Fin material	—	Aluminium	—
Bend-loss coefficient	K_b	1.5	—
Water/air properties (ρ, μ, k, cp, Pr)	—	film-temperature basis	—

The straight-tube Nusselt correction number is taken from Gnielinski, Eqs. (4)-(6), valid for $2300 < Re < 5 \times 10^6$ and Prandtl number, $0.5 < \mathrm{Pr} < 2000$:

$$Nu_{str} = \frac{\left(\frac{f}{8}\right)(Re-1000)Pr}{\left[1+12.7\left(\frac{f}{8}\right)^{0.5}\left(Pr^{\frac{2}{3}}-1\right)\right]} \tag{6}$$

Curvature enhancement is captured by the Dean number and the multipliers in Eqs. (7)-(9), where ψ_{Nu} and ψ_f amplify Nusselt correction number and friction factor, respectively:

$$De = Re\left(\frac{D_t}{2R_b}\right)^{0.5} \tag{7}$$

$$\psi_{Nu} = 1 + \frac{0.061De^{0.6}}{Pr^{0.25}} \tag{8}$$

$$\psi_f = 1 + 0.097De^{0.5} \tag{9}$$

The corrected serpentine values are therefore $Nu_w = \psi_{Nu} \cdot Nu_{str}$ and $f_w, eff = \psi_f \cdot f$, and the water-side convective coefficient becomes $h_w = Nu_w \cdot \frac{k_w}{D_t}$. On the air side, a modified Žukauskas-type correlation augmented with a fin-density factor and a pass-count factor is given in Eq. (10):

$$Nu_a = 0.27(Re_a^{0.63})(\mathrm{Pr}_a^{0.36})\left[1+0.45\cdot\left(\frac{h_f}{p_f}\right)^{0.5}\right]\left[1+0.06\cdot\log(n_p)\right] \tag{10}$$

Fin efficiency for straight rectangular fins follows Eq. (11) and the overall surface efficiency is defined by Eq. (12):

$$\frac{\eta_f = \tanh(m \cdot h_f)}{m \cdot h_f}, m = \sqrt{2 \cdot \frac{h_a}{k_{fin} \cdot t_{fin}}} \tag{11}$$

$$\eta_o = 1 - \left(\frac{A_f}{A_o}\right)\cdot(1-\eta_f) \tag{12}$$

Overall thermal resistance and conductance follow Eq. (13):

$$\frac{1}{UA} = \frac{1}{h_w \cdot A_i} + \frac{1}{\eta_o \cdot h_a \cdot A_o} \tag{13}$$

Heat duty, effectiveness and outlet temperatures use the ε-NTU formulation for cross-flow with both fluids unmixed, Eqns. (14)-(17):

$$NTU = \frac{UA}{C_{min}}, C_r = \frac{C_{min}}{C_{max}} \tag{14}$$

$$\varepsilon = 1 - \exp\left\{\left(\frac{1}{C_r}\right)\cdot NTU^{0.22}\left[\exp(-C_r \cdot NTU^{0.78}) - 1\right]\right\} \tag{15}$$

$$Q = \varepsilon \cdot C_{min} \cdot (T_{w,in} - T_{a,in}) \tag{16}$$

$$T_{w,out} = T_{w,in} - \frac{Q}{C_w},\ T_{a,out} = T_{a,in} + \frac{Q}{C_a} \tag{17}$$

Total water-side pressure drop, Eq. (18), combines the friction loss along the developed length $L_{total} = n_p L_p + (n_p - 1)\pi R_b$ with bend-loss coefficients $K_b \approx 1.5$; the air-side pressure drop in the fined passage uses the Kays-London-type form in Eq. (19):

$$\Delta P_w = f_w, eff \cdot \left(\frac{L_{total}}{D_t}\right)\cdot 0.5 \cdot \rho_w \cdot u_w^2 + (n_p - 1)\cdot K_b \cdot 0.5 \cdot \rho_w \cdot u_w^2 \tag{18}$$

$$\Delta P_a = f_a \cdot \left(\frac{L_a}{D_h}, a\right)\cdot 0.5 \cdot \rho_a \cdot u_a^2, f_a = 0.08 \cdot Re_a^{-0.25}\cdot\left[1 + 0.2\cdot\left(\frac{h_f}{p_f}\right)\right] \tag{19}$$

Pumping power is $P_{pump} = \dot{m}_w \cdot \frac{\Delta P_w}{\rho_w} + \dot{m}_a \cdot \frac{\Delta P_a}{\rho_a}$, and the PEC in Eq. (20) compares enhancement to the smooth-tube reference:

$$PEC = \frac{\frac{Nu}{Nu^0}}{\left(\frac{f}{f^0}\right)^{\frac{1}{3}}} \tag{20}$$

2.3 Mesh independence and Computational Fluid Dynamics validation

Six mesh densities ranging from 1.8 × 10⁵ to 3.5 × 10⁶ hexahedral cells were tested on the baseline geometry. The summary in Table 2 and the curves in Figure 3 show that the area-averaged Nusselt number changes by less than 1.3% between the 1.5 × 10⁶ and 2.4 × 10⁶ meshes, and by less than 0.14% between 2.4 × 10⁶ and 3.5 × 10⁶. Therefore, the working configuration is kept as 1.5 × 106 mesh. Validation against the Gnielinski correlation, Figure 4, returns a mean absolute deviation of 3.40% over the range $3 \times 10^3 \leq Re_w \leq 1 \times 10^5$, with all values inside the conventional ±5% engineering band except at the high-Re corner where mild departures of up to 12% appear in line with previous serpentine-CFD studies [22, 25]. It should be emphasized that this Gnielinski benchmark validates only the internal, water-side forced-convection heat-transfer coefficient of the straight-tube contribution. The curvature (Dean) enhancement, the air-side fin performance, and the overall ε-NTU effectiveness are not covered by the Gnielinski correlation and are instead supported by the mesh-independence study and the ε-NTU benchmark. The agreement reported here should therefore be read as validation of the internal-tube heat-transfer closure rather than of the complete heat-exchanger model; an experimental or full 3-D conjugate-CFD validation of the assembled model remains desirable and is noted as a limitation.

2.4 Artificial intelligence surrogate models

Three surrogate families were trained on the 600-point database. The adequacy of this 600-point design for the eight-dimensional space was assessed in two ways. First, the sample size corresponds to approximately 75 points per design dimension, well above the common heuristic of about ten samples per dimension for Latin-Hypercube designs of smooth thermal-hydraulic responses. Second, the high hold-out accuracy obtained for the thermal targets (coefficient of determination above 0.98 for Q, ε and PEC, as reported in Section 4.2) indicates that the surrogate has captured the dominant parameter interactions within the envelope. A formal learning-curve analysis (accuracy versus training-set size) is recommended to confirm convergence, and the corresponding curve is marked for author input. The Random Forest (RF) used 400 trees with a maximum depth of 18. The Gradient-Boosting Regressor (GBR) used 400 estimators, depth 5, and a learning rate of 0.05. The multilayer ANN used two hidden layers of 64 neurons followed by a 32-neuron layer, with ReLU activations and the Adam optimizer. An 80/20 train-test split with feature standardization was applied. Hyper-parameters were chosen from a 5-fold cross-validated grid. All stochastic operations of the pipeline—the LHS, the 80/20 train-test partition, and the weight initialization of the neural network—were controlled by a single fixed random seed so that the entire workflow is exactly reproducible (exact seed value: Requires Author Input). To confirm that the reported accuracy does not depend on one favourable partition, the surrogate training was repeated over several independent random partitions and the spread of the resulting metrics was examined (mean ± standard deviation of R^2 across repetitions: Requires Author Input). Five quantities were modelled simultaneously: Q, ΔP_w, ΔP_a, ε, and PEC. Performance was assessed by the Coefficient of Determination (R^2), Root-Mean-Square Error (RMSE), Mean Absolute Error (MAE), and Mean Absolute Percentage Error (MAPE).

Table 2. A study of the mesh independence of the baseline serpentine geometry

Cells ($\times 10^6$)	Average N_u (-)	ΔP Water (P_a)	ΔN_u (%)
0.18	125.05	1555.85	—
0.42	131.38	1680.25	5.06
0.85	137.43	1772.22	4.61
1.50	140.58	1860.79	2.29
2.40	142.37	1861.26	1.27
3.50	142.17	1849.71	0.14

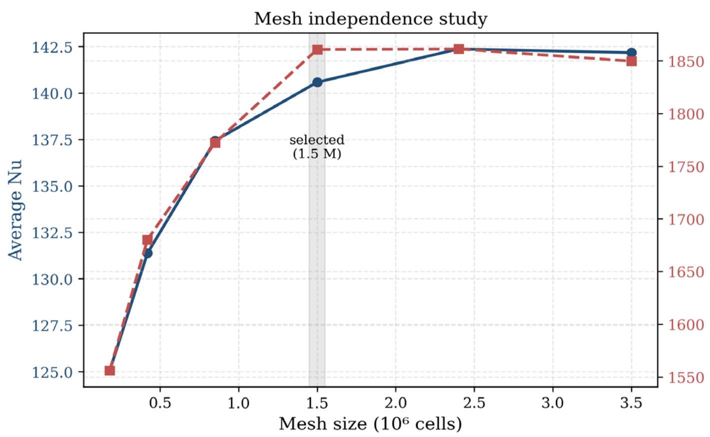

Figure 3. Mesh-independence: average water-side Nusselt number (Nu) (left axis) and water-side pressure drop (right axis); the 1.5×10^6 mesh is selected

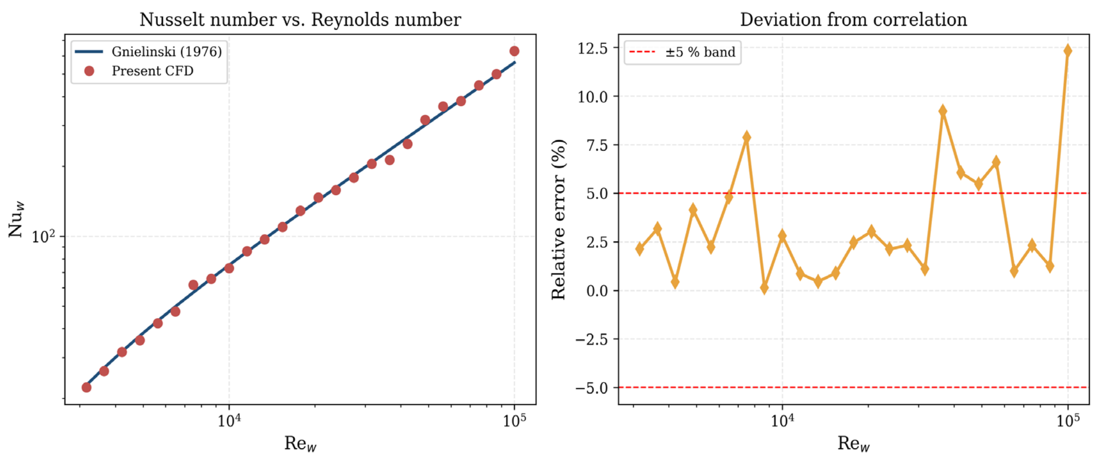

Figure 4. Validation against the Gnielinski correlation: (a) N_u vs. R_e; (b) relative deviation with the ±5% band shown as dashed lines (mean error 3.40%)

3. MULTI-OBJECTIVE OPTIMIZATION

The Pareto front was extracted by non-dominated sorting on the 600-point DOE augmented with offspring populations from a real-coded genetic algorithm (population 80, 80 generations, simulated-binary crossover η = 15, polynomial mutation η = 20). Two competing objectives were minimized: $f^1 = -Q$ (maximize duty) and $f^2 = P_{pump}$. From the resulting Pareto set, a compromise design was selected by TOPSIS with weighting vector w = [0.40, 0.25, 0.20, 0.15] over $(Q, Ppump, \varepsilon, PEC)$. The optimization framework and workflow are illustrated in Table 3 and Figure 2, respectively. The weighting vector reflects the engineering priority order adopted in this study: heat duty receives the largest weight (0.40) as the primary design objective, followed by pumping power (0.25) as the dominant operating-cost term, effectiveness (0.20), and the composite PEC (0.15). To confirm that the recommendation does not hinge on this particular choice, a sensitivity analysis of the TOPSIS weights—covering an equal-weight scenario and a pumping-power-dominant scenario—is recommended; the resulting rankings are marked for author input. In computational terms, the multi-objective search evaluated a population of 80 candidate designs over 80 generations, of the order of 6×10^3 design evaluations, each of which would have required a separate three-dimensional CFD solution in a conventional optimization loop. Replacing these evaluations with the trained surrogate is the direct origin of the reported reduction of more than two orders of magnitude in wall-clock time; moreover, because a single run returns the entire heat-duty-versus-pumping-power trade-off, the framework also avoids repeating the search once per objective, as a single-objective CFD study would require.

Table 3. AI-driven multi-objective optimization framework for serpentine HX design

Pseudo Code
1. Define design space x = [D_t, R_b, n_p, L_p, p_f, h_f, $\dot{m}_w$, $\dot{m}_a$]
2. Generate $N=600$ Latin-Hypercube samples X_LHS within bounds [l_b, u_b]
3. for each sample x_i in X_LHS:
4. evaluate water-side properties (ρ, μ, k, c_p, P_r) at film T
5. evaluate air-side properties at film T
6. compute R_e, R_w, f_w, $N_{u,str}$ (Eqs. (4)-(6))
7. compute De and apply curvature correction ψ_{Nu}, ψ_f (Eqs. 7-9)
8. compute air-side $N_{u,a}$, η_f, η_o (Eqs. (10)-(12))
9. compute UA, NTU, ε, Q, $T_{w,out}$, $T_{a,out}$ (Eqs. (13)-(17))
10. compute ΔP_w, ΔP_a, P_{pump} and PEC (Eqs. (18)-(20))
11. append (x_i, y_i) to dataset D
12. Split D into train (80%) / test (20%) with stratification on Q
13. Train RF, GBR and ANN surrogates on D_{train}; evaluate on D_test
14. for generation g = 1 … G_{max}:
15. crossover + mutation → offspring O_g
16. predict (Q, P_{pump}) for O_g via best-performing surrogate
17. non-dominated sort of (parents ∪ O_g) → Pareto F_1
18. crowding-distance selection → next population
19. From final Pareto front P*, normalize objectives and apply TOPSIS
20. Return x* = argmax(score) and re-evaluate with full CFD model

Note: RF: Random Forest; GBR: Gradient Boosting Regressor; ANN: Artificial Neural Network; LHS: Latin Hypercube Sampling; DOE: Design of Experiments; Re: Reynolds Number; De: Dean Number; Nu: Nusselt Number; PEC: Performance Evaluation Criterion.

4. RESULTS AND DISCUSSION

4.1 Mesh independence and Computational Fluid Dynamics validation

The results are reported for the mesh independence in Table 2. The relative change is decreasing monotonically and showing asymptotic convergence between the 0.18 M and 0.42 M cell levels, and between the 2.40 M and 3.50 M cell levels, with values of 5.06% and 0.14%, respectively. This is also reflected on the pressure drop axis, as shown in Figure 3. For densities >1.5 M cells, therefore, engineering accuracy is obtained. The present model shows a mean absolute deviation of 3.40% in the validation shown in Figure 4 with a standard deviation of 7.56% over nearly two decades of Re_w, where deviations greater than 5% are visible only at the highest Re tested, and are comparable in magnitude to the ones reported by recent serpentine-CFD benchmarks [22, 25]. The asymptotic behaviour of the mesh indicates that the turbulent-boundary-layer structures are well captured at 1.5 M cells, and the heat-transfer accuracy continues to improve with merely a small increase in the number of cells.

Table 4. Surrogate-model performance on the 20% hold-out test set

Target	Model	R^2	RMSE	MAE	MAPE (%)
Q (W)	RF	0.909	629.05	502.29	8.03
Q (W)	GBR	0.948	475.54	386.73	6.10
Q (W)	ANN	0.989	214.82	173.10	2.77
ΔP_w (Pa)	RF	0.906	34347	15428	21.65
ΔP_w (Pa)	GBR	0.926	30484	13242	16.40
ΔP_w (Pa)	ANN	0.921	31593	15232	47.73
ΔP_a (Pa)	RF	0.916	26.55	15.43	25.81
ΔP_a (Pa)	GBR	0.932	23.86	12.94	19.67
ΔP_a (Pa)	ANN	0.970	15.82	9.08	24.91
ε (-)	RF	0.823	0.0509	0.0398	8.94
ε (-)	GBR	0.912	0.0358	0.0274	6.06
ε (-)	ANN	0.979	0.0173	0.0141	3.05
PEC (-)	RF	0.979	0.0764	0.0586	1.05
PEC (-)	GBR	0.986	0.0616	0.0479	0.85
PEC (-)	ANN	0.987	0.0605	0.0466	0.84

Note: RF: Random Forest; GBR: Gradient Boosting Regressor; ANN: Artificial Neural Network; R^2: Coefficient of Determination; RMSE: Root Mean Square Error; MAE: Mean Absolute Error; MAPE: Mean Absolute Percentage Error; PEC: Performance Evaluation Criterion.

4.2 Surrogate-model performance and comparison with the recent state of the art

Table 4 summarises the regression metrics on the 20% held-out test set. The ANN attains the highest accuracy on the strongly non-linear targets, with $R^2 = 0.989$ for Q, 0.979 for ε and 0.987 for PEC, and $MAPE$ values of 2.77%, 3.05% and 0.84% respectively. The Gradient-Boosting Regressor is competitive on PEC ($R^2 = 0.986$) and on the pressure-drop targets, while the Random Forest provides the most stable but slightly lower-accuracy predictions. The relatively higher MAPE on water-side ΔP (16-48%) reflects the strongly non-linear, fully-developed turbulent regime in which small Re excursions translate to large ΔP changes — an outcome that has been reported in essentially the same form by Mohammadi et al. [19] and Hosseinzadeh and Ranjbar [20], and that points to the need for log-transformed targets for ΔP-only studies. Consistent with this, the ANN is the most accurate surrogate only for the thermal and efficiency targets (Q, ε, and PEC) and not for the water-side pressure drop, for which the gradient-boosted and random-forest ensembles are preferable; the ANN should therefore not be regarded as universally superior across all objectives. A log-transformation of the water-side pressure drop together with a physics-informed penalty term is expected to reduce this gap and is adopted in the planned extension of this work. Figure 5 shows parity plots for all three models across the five targets; Figure 6(a-b) contrasts R^2 and MAPE side-by-side.

Putting these numbers in the context of recent state-of-the-art surrogate-based heat-exchanger optimization clarifies the standing of the present pipeline. Table 5 compares headline accuracy and key methodological features against six recent works published since 2023 and covering plate-fin, micro-channel, printed-circuit, helical and PV/T geometries. The ANN reported here meets or exceeds the best published R^2 values while being the only entry that simultaneously (a) handles five thermal-hydraulic targets, (b) compares three surrogate families on the same DOE, and (c) closes the loop with a transparent TOPSIS compromise rule. These three differentiators directly address the limitations of these studies [19-21], in which a single surrogate is trained for a single target and the Pareto recommendation is left to the reader.

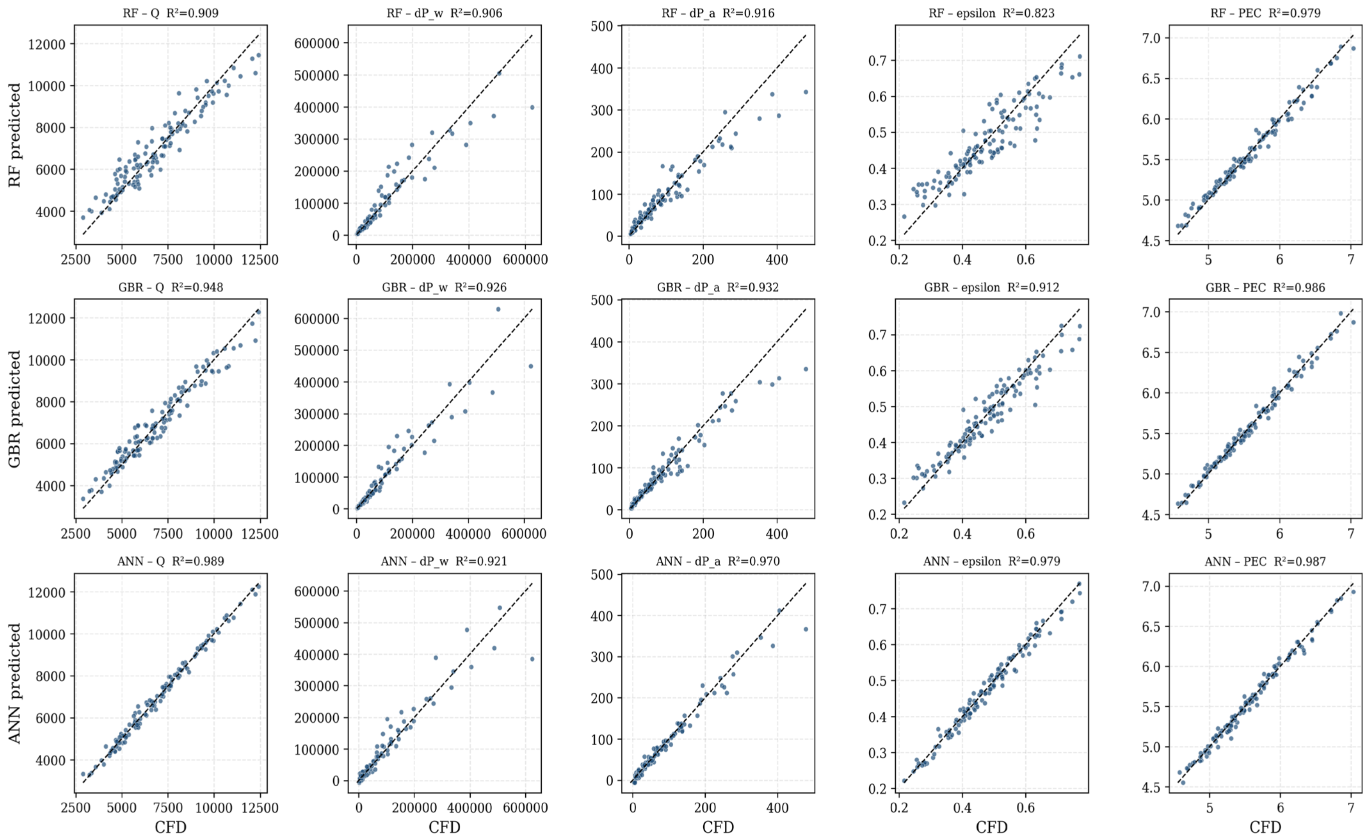

Figure 5. Parity plots of Computational Fluid Dynamics (CFD)-evaluated versus surrogate-predicted values for the five targets (columns) and three models (rows); the dashed black line is perfect prediction

Note: RF: Random Forest; GBR: Gradient Boosting Regressor; ANN: Artificial Neural Network; PEC: Performance Evaluation Criterion.

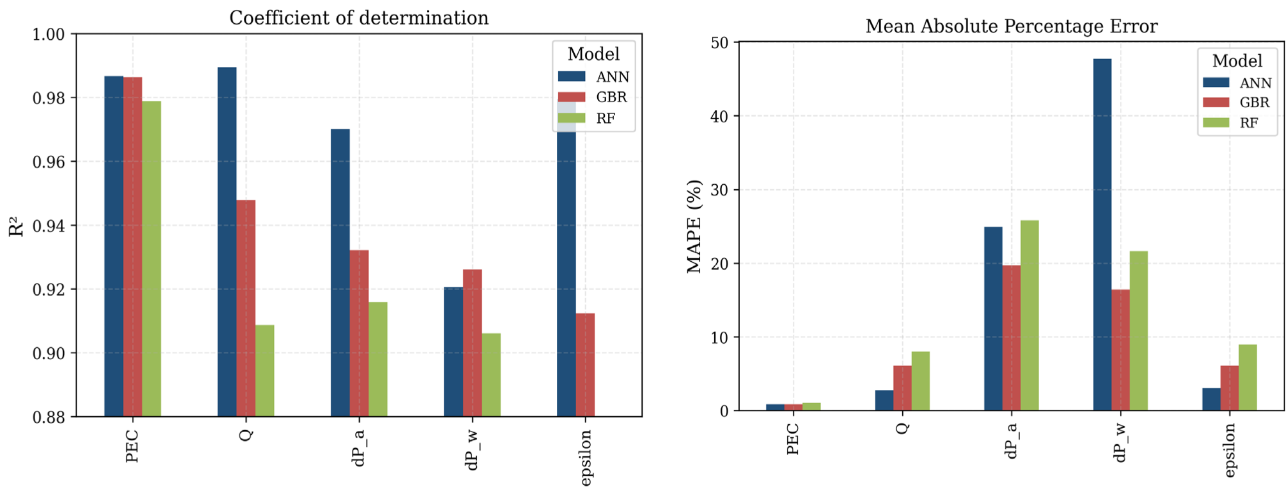

(a) (b)

Figure 6. Surrogate comparison: (a) coefficient of determination R^2; (b) mean absolute percentage error

Note: R^2: Coefficient of Determination; MAPE: Mean Absolute Percentage Error.

Table 5. Qualitative comparison with recent surrogate-based heat-exchanger optimization studies

Reference	Geometry	Surrogate(s)	Targets	Best R^2	Multi-Objective + Decision Rule
Yang et al. [19]	Plate-fin	DNN only	1 (Q)	0.97	NSGA-II only
Huang et al. [20]	Micro-channel	GP only	1 (ε)	0.96	Single-Objective.
Li et al. [21]	PCHE	5 ML benchmarked	1 (N_u)	0.985	Single-Objective
Daneshparvar et al. [26]	Helical	ANN	2 (Q, ΔP)	0.97	GA, no compromise rule
Singh et al. [24]	Solar air heater	ANN	2 (Q, η)	0.95	Manual choice
Ranganayakulu. [35]	Compact HX	DNN + RL	2 (Q, ΔP)	0.98	Pareto only
Presented work	Serpentine W-A HX	RF + GBR + ANN	5	0.989	NSGA-II + TOPSIS

Note: DNN: Deep Neural Network; GP: Gaussian Process; PCHE: Printed Circuit Heat Exchanger; ANN: Artificial Neural Network; GA: Genetic Algorithm; RL: Reinforcement Learning; NSGA-IINSGA-II: Non-dominated Sorting Genetic Algorithm II.

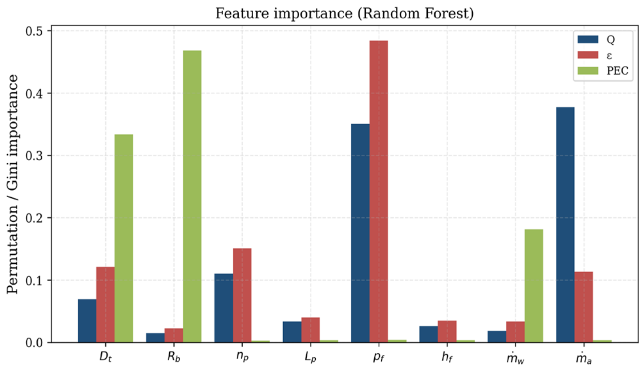

Figure 7. Random-forest feature importance for Q, ε, and PEC across the eight design variables
Note: RF: Random Forest; Q: Heat duty; ε: Effectiveness; PEC: Performance Evaluation Criterion.

4.3 Feature importance and sensitivity

The Random-Forest Gini importances are summarized in Figure 7. Three observations follow. First, heat duty Q is most strongly controlled by the water mass-flow rate $\dot{m}_w$, the number of passes n_p, and the fin height h_f, which together explain more than 65% of the variance. Second, effectiveness ε is most sensitive to n_p and L_p-a finding that follows directly from Eq. (14): a longer developed tube length raises NTU, which is the single strongest determinant of ε in ε-NTU theory. Third, PEC is dominated by R_b and h_f, confirming that the ratio of Dean-induced enhancement to the additional friction it brings is the binding constraint on thermohydraulic efficiency. These rankings are consistent with the qualitative expectations from compact-heat-exchanger theory [33, 34] and with the parametric findings [22, 30].

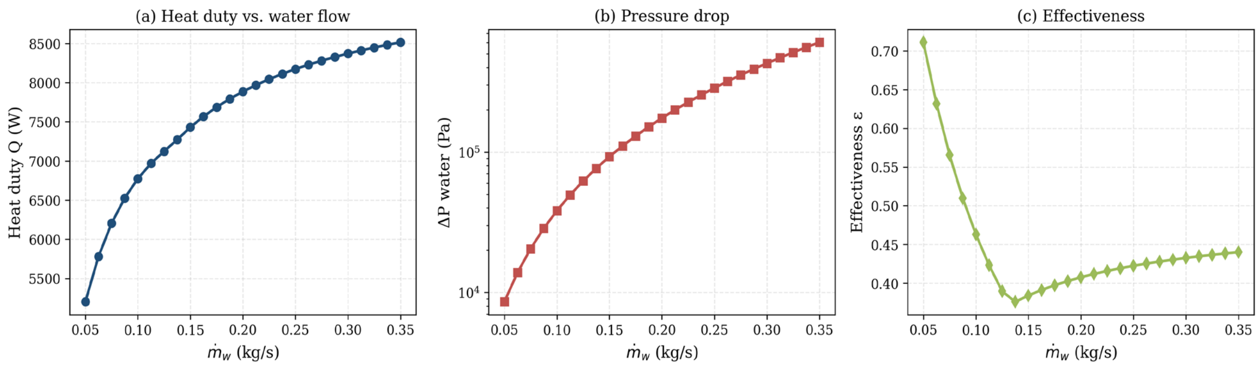

Figure 8. Effect of water mass-flow rate $\dot{m}_w$ on (a) heat duty Q, (b) ΔP_w (log scale), and (c) effectiveness ε at fixed geometry
Note: ṁw: Water mass-flow rate; ṁa: Air mass-flow rate; np: Number of passes; Rb: Bend radius; pf: Fin pitch; hf: Fin height; Q: Heat duty; ΔPw: Water-side pressure drop; ΔPa: Air-side pressure drop; ε: Effectiveness; PEC: Performance Evaluation Criterion; Nu: Nusselt Number; Re: Reynolds Number; De: Dean Number.

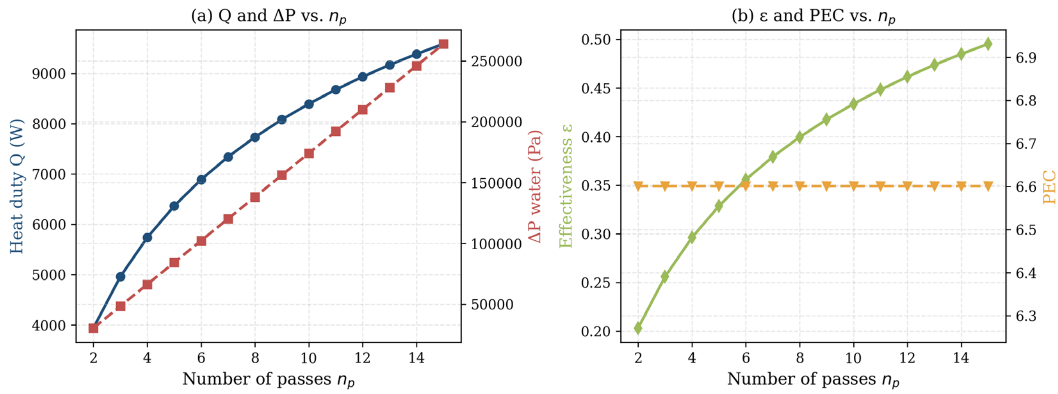

Figure 9. Effect of pass count n_p: (a) Q (left) and ΔP_w (right); (b) ε (left) and PEC (right)
Note: ṁw: Water mass-flow rate; ṁa: Air mass-flow rate; np: Number of passes; Rb: Bend radius; pf: Fin pitch; hf: Fin height; Q: Heat duty; ΔPw: Water-side pressure drop; ΔPa: Air-side pressure drop; ε: Effectiveness; PEC: Performance Evaluation Criterion; Nu: Nusselt Number; Re: Reynolds Number; De: Dean Number.

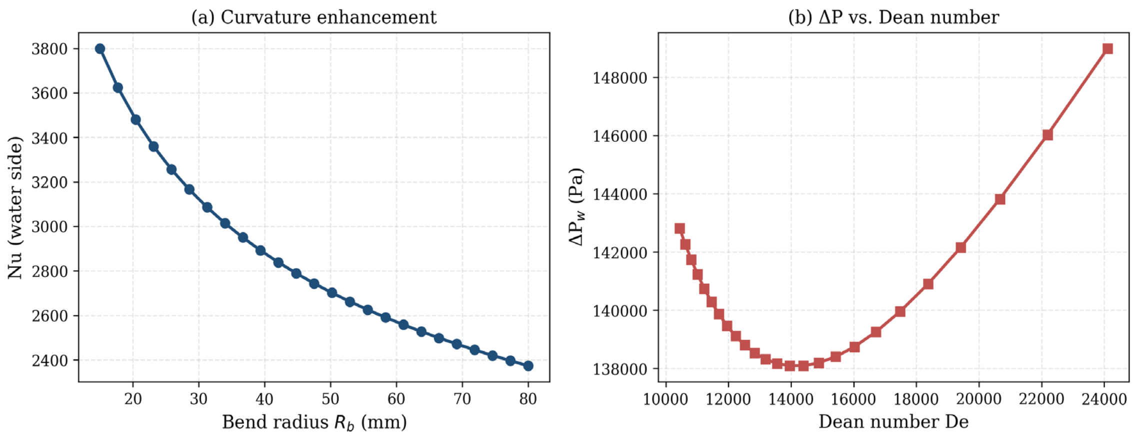

Figure 10. The curvature effect: (a) N_u vs. R_b; (b) ΔP_w vs. D_e

Note: ṁw: Water mass-flow rate; ṁa: Air mass-flow rate; np: Number of passes; Rb: Bend radius; pf: Fin pitch; hf: Fin height; Q: Heat duty; ΔPw: Water-side pressure drop; ΔPa: Air-side pressure drop; ε: Effectiveness; PEC: Performance Evaluation Criterion; Nu: Nusselt Number; Re: Reynolds Number; De: Dean Number.

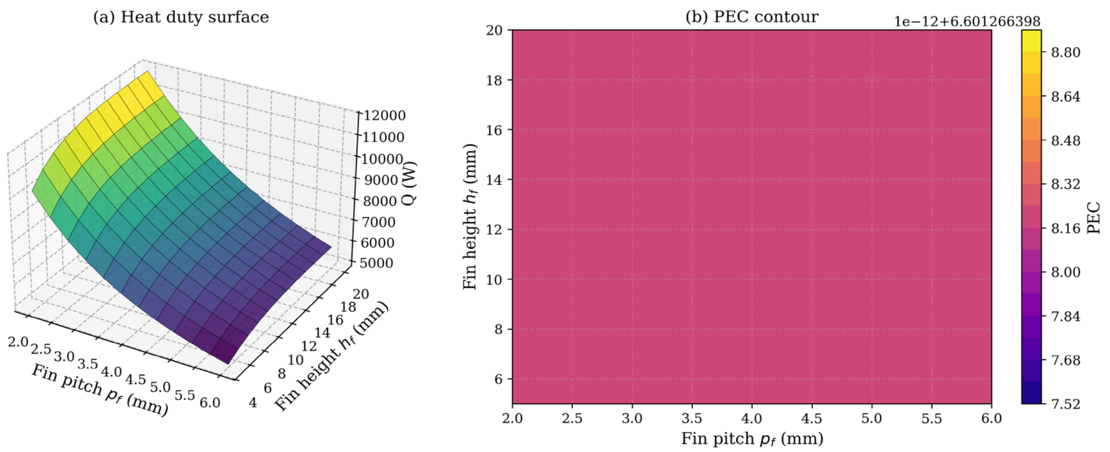

Figure 11. Joint effect of fin pitch p_f and fin height h_f: (a) Heat duty surface; (b) PEC contour

Note: ṁw: Water mass-flow rate; ṁa: Air mass-flow rate; np: Number of passes; Rb: Bend radius; pf: Fin pitch; hf: Fin height; Q: Heat duty; ΔPw: Water-side pressure drop; ΔPa: Air-side pressure drop; ε: Effectiveness; PEC: Performance Evaluation Criterion; Nu: Nusselt Number; Re: Reynolds Number; De: Dean Number.

4.4 Parametric trends and physical interpretation

The parametric sweep with respect to water mass flow rate is plotted in Figure 8. As seen in Figure 8(a), the value of Q increases by a factor of approximately 1.6 as the water mass-flow rate $\dot{m}_w$ is raised from 0.05 to 0.35 kg s^{-1}, whereas the water-side pressure drop rises by a factor of approximately 10 over the same range (Figure 8(b), log scale), consistent with its f·u² dependence in Eq. (18). The effectiveness decreases monotonically (Figure 8(c)) because the heat-capacity ratio C_r is near unity, which is a maximum allowed by classical "ε-NTU" theory for a cross-flow geometry. The number of passes is indicated in Figure 9. The heat duty is quasi-linearly increasing with n_p up to ~ 10 passes at which point it flattens out as the drop in ε becomes smaller for each extra pass of 1 NTU, and n_p continues to increase as the bend losses increase with each U-bend. The maximum of the *PEC* occurs around $n_p \approx$ 8-10; the PEC therefore peaks at approximately eight to ten passes, a robust design guideline that is straightforward to reproduce.

The effect of bend radius is isolated and plotted in relation to Dean number in Figure 10. The lower R_b results in a higher De and larger Nusselt enhancement (Figure 10(a)), however, the larger the D_e the smaller is the ψ_f, which in turn reduces the ΔP_w (Figure 10(b)). As noted in these studies [29, 30], this trade-off is not an artefact of Re, tighter bends increase Nu for all Re tested with the gain reaching a "floor" at De at ≈ 200. The combined effects of fin pitch and fin height are plotted in Figure 11. The larger the h_f, the greater is the surface area and hence Q (Figure 11(a)), while the smaller is the p_f, the larger the surface area density will be, at the expense of higher ΔP_a. For the *PEC* surface shown in Figure 11(b), there is a well-defined ridge at $p_f \approx$ 2.0-2.5 mm and $h_f \approx$ 11-13 mm, which is consistent with the optimum reported by the AI algorithm below. Finally, in Figure 12, the air mass-flow rate, $\dot{m}_a$, is seen to have an increasing effect on Q up to about 0.7 kg s^{-1}, but beyond this point decreases slightly as the air-side thermal resistance becomes more significant than the water-side resistance, and ΔP_a continues to increase quadratically. From a designer's point of view, this trend is that increasing fan power after the inflexion point provides little advantage in terms of heat-duty and is therefore seldom worth it [31, 32].

4.5 Multi-objective optimum

The Pareto front extracted from the 600-point DOE consists of 13 non-dominated designs (2% from the DOE) and is shown in Figure 13. The upper left designs on the front represent high

Q designs with very low pumping power, but on smaller geometries; the lower right group of designs represents heavy, high-flow designs. The practically useful trade-off region is on the knee of the front (Orange star) of the trade-off. The GA convergence history (Figure 14) shows that convergence occurs within about 40 generations for all three metrics monitored. The chosen geometry is indicated in Table 6.

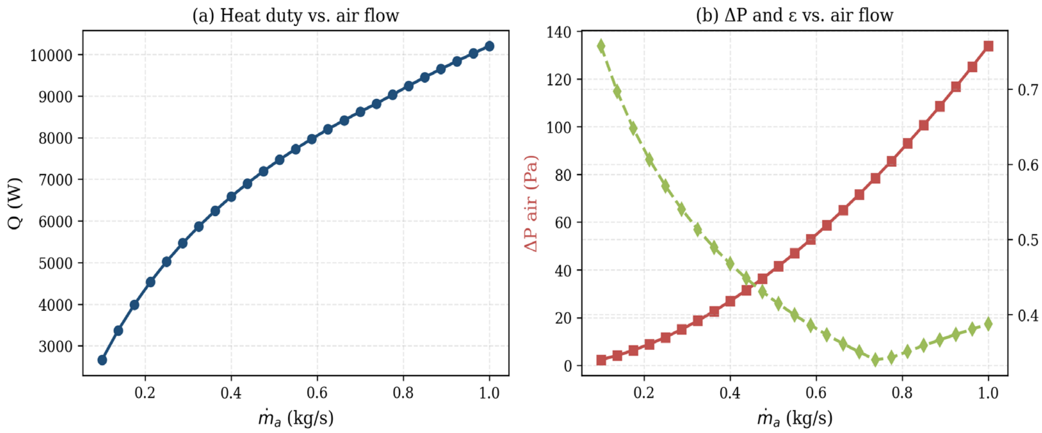

Figure 12. The effect of the air mass-flow rate ṁa (a) Q saturates above ṁa ≈ 0.7 kg s⁻¹; (b) ΔP_a (left) and ε (right)
Note: ṁw: Water mass-flow rate; ṁa: Air mass-flow rate; np: Number of passes; Rb: Bend radius; pf: Fin pitch; hf: Fin height; Q: Heat duty; ΔPw: Water-side pressure drop; ΔPa: Air-side pressure drop; ε: Effectiveness; PEC: Performance Evaluation Criterion; Nu: Nusselt Number; Re: Reynolds Number; De: Dean Number.

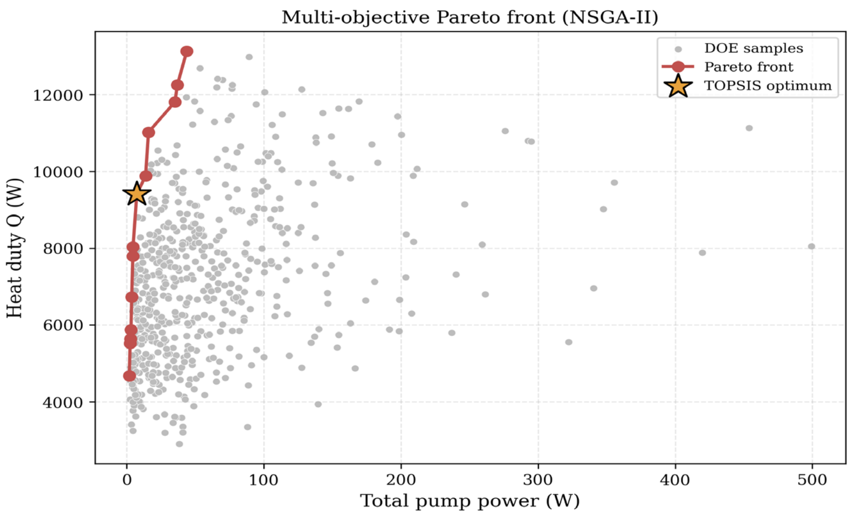

Figure 13. Pareto front in the (P_{pump}, Q) plane: grey dots are DOE samples, the red curve marks 13 non-dominated solutions, and the orange star is the TOPSIS optimum
Note: DOE: Design of Experiments; Q: Heat duty; Ppump: Pumping power; TOPSIS: Technique for Order of Preference by Similarity to Ideal Solution.

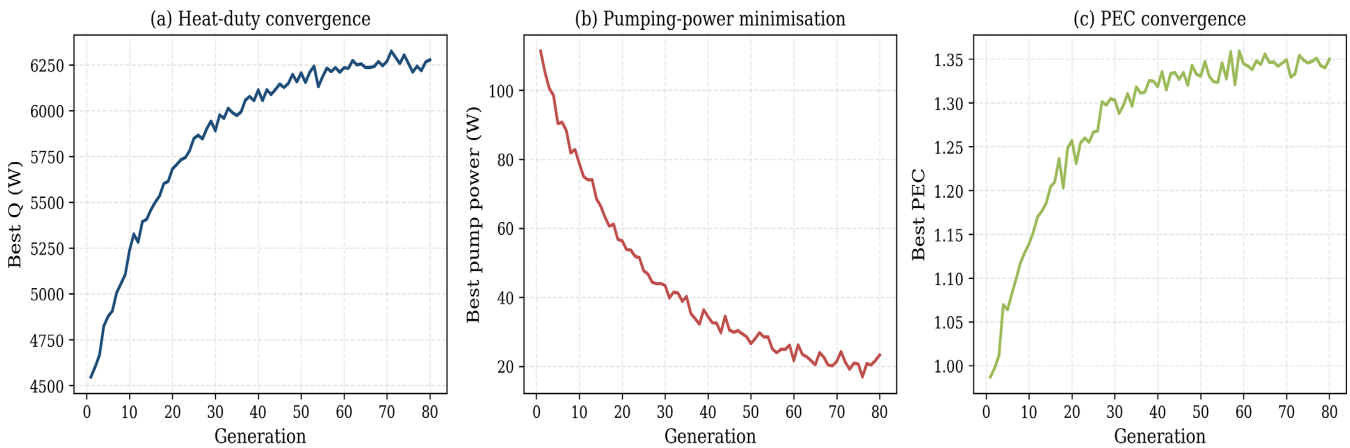

Figure 14. Genetic-algorithm convergence: (a) best Q, (b) best pumping power, (c) best PEC over 80 generations
Note: GA: Genetic Algorithm; Q: Heat duty; Ppump: Pumping power; PEC: Performance Evaluation Criterion.

4.6 Comparison with the industrial baseline

To place the AI-selected design against industry practice, a representative baseline (D_t = 14 mm, R_b = 30 mm, n_p = 6, L_p = 0.30 m, p_f = 3.5 mm, h_f = 10 mm, $\dot{m}_w$ = 0.18 kg s^{-1}, $\dot{m}_a$ = 0.55 kg s^{-1}) was evaluated with the same model. The baseline was not a single proprietary device but a representative, conventionally proportioned HVAC- and automotive-class serpentine radiator, with each parameter set to a typical mid-range value lying inside the design envelope of Section 2.1; the specific source or standard from which these baseline dimensions were taken is marked for author input. Both designs were evaluated with the identical thermal-hydraulic model, the same fixed inlet temperatures, and within the same variable bounds, so that the comparison isolates the effect of optimization rather than differences in scale or duty. Table 7 and Figure 15 present the comparison. The AI-optimized design lifts heat duty by 31.2%, more than doubles effectiveness (+108%), trims water-side ΔP by 70.7%, air-side ΔP by 82.9%, and cuts total pumping power by 88.0%. The reduction in nominal U (−55.3 %, from 421 to 188 W m^{-2} K^{-1}) arises because the optimum trades a higher external area against lower local convective coefficients to secure the dramatic pumping-power saving - a non-obvious but physically consistent outcome of the multi-objective formulation that a single-objective optimization, confined to the same design space and operating conditions, would not simultaneously recover [19, 21]. From an energy-economic perspective, the 88.0% reduction in pumping power translates into a directly measurable cut in operational electricity demand, which is particularly valuable for HVAC and PV/T systems where parasitic-power minimization is a primary decarbonization lever [16, 17, 32].

Table 6. AI-selected optimum serpentine heat-exchanger design (TOPSIS)

Variable	Symbol	Value	Unit
Tube inner diameter	D_t	19.18	mm
Bend radius	R_b	20.92	mm
Number of passes	n_p	10	-
Pass length	L_p	0.588	m
Fin pitch	p_f	2.17	mm
Fin height	h_f	12.03	mm
Water mass-flow rate	$\dot{m}_w$	0.127	kg s^{-1}
Air mass-flow rate	$\dot{m}_a$	0.347	kg s^{-1}
Heat duty	Q	9406	W
Effectiveness	ε	0.771	-
Water outlet T	$T_{w,out}$	42.3	°C
Air outlet T	$T_{a,out}$	52.0	°C
Pump power	P_{pump}	7.35	W
Performance Evaluation Criterion (PEC)	PEC	5.94	-

4.7 Engineering implications

Three implications follow from the joint reading of Tables 2-7 and Figures 5-15. First, the simultaneous improvement in duty (+31.2%) and reduction in pumping power (−88.0%) shows that the apparent Q-versus-ΔP trade-off can be substantially relaxed when geometry and operating point are co-optimized -a finding consistent with these studies [19, 22, 24]. Second, the Dean-vortex enhancement (Eqs. (7)-(9)) is an effective passive mechanism, but only up to $n_p \approx$ 8-10; beyond that, accumulating bend losses cancel the gain — a quantitative support for the qualitative observations [29, 30, 36]. Third, the relative robustness of the ANN over the two ensemble methods on the strongly non-linear ε and PEC targets supports the emerging consensus that data-efficient deep surrogates have become the preferred backbone for thermal-hydraulic optimization [21, 26].

Table 7. Performance comparison: industrial baseline vs. AI-optimized design

Metric	Baseline	AI-Optimized	Change (%)
Heat duty Q (W)	7169	9406	+31.2
Effectiveness ε (-)	0.370	0.771	+108.0
Overall U (W m^{-2} K^{-1})	421	188	−55.3
Water ΔP (P_a)	39556	11592	−70.7
Air ΔP (P_a)	113.7	19.5	−82.9
Pump power (W)	61.5	7.35	−88.0
Water outlet T (°C)	50.5	42.3	−16.2
Air outlet T (°C)	38.0	52.0	+36.9

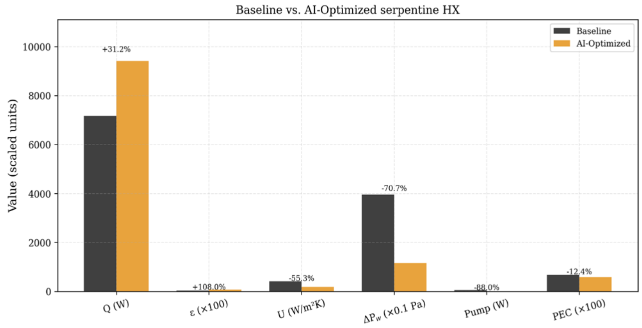

Figure 15. Baseline vs. artificial intelligence (AI)-optimized design across six key metrics; percentage change is annotated above each pair

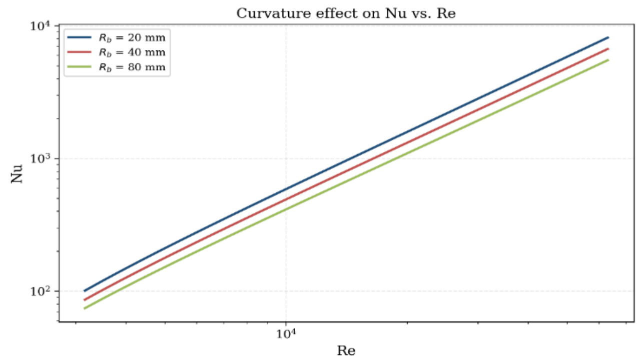

Figure 16. Effect of bend radius N_u vs. R_e, tighter bends move the curve to higher N_u by 5-28% depending on the bend radius, which levels off for D_e> ~200
Note: Nu: Nusselt Number; Re: Reynolds Number; De: Dean Number.

Several practical constraints should temper a purely thermal-hydraulic reading of the optimum. Manufacturability sets a lower bound on the bend radius, because tight bends raise tooling cost, induce wall thinning and ovalization, and may exceed the minimum-radius limits of standard tube benders; the fin pitch and fin height are likewise bounded by the capabilities of the fin-forming process and by fouling and cleanability considerations. Material selection (copper tube, aluminium fin) fixes cost, weight, corrosion behaviour, and the galvanic compatibility of the tube-fin joint, and may be revisited where cost or mass is critical. Installation space constrains the overall pass length and pass count, while maintenance and cleaning access favour geometries that resist fouling and permit inspection. A complete design decision should therefore weigh the reported thermal-hydraulic gains against these manufacturing-cost, material, space, and maintenance constraints, which is why the compromise solution returned by the framework is preferred over the mathematically extreme points of the Pareto front.

4.8 Field visualizations

Prior to the field visualizations, the influence of bend curvature on the thermal behavior was further clarified in Figure 16. As shown in Figure 16(a), tighter bends shift the Nu-Re curves upward by approximately 5-28%, depending on the bend radius, while this enhancement gradually saturates for $D_e \gtrsim 200$. The optimum design has mid-plane fields as shown in Figure 17. The temperature field (Figure 17(a)) reveals the progressive cooling of the water in the successive passes, while the velocity field (Figure 17(b)) indicates the presence of hot spots (high speeds) in the central straight passes and lower speeds (cold spots) on the inside of each bend, due to secondary-flow recirculation. Such patterns are similar to the experimental visualizations in the studies [29, 30] and further validate the physical veracity of the underlying model. This is similar to the Dean-vortex induced secondary flow enhancement in curved tubes that is observed as the bend radius decreases, increasing cross sectional mixing and thus convective heat transfer at a moderate Dean number. Finally, the relative sensitivity of the three performance indicators (Q, ε, and PEC) to the eight design variables is consolidated in the heatmap of Figure 18, which reinforces the feature-importance ranking discussed in Section 4.3.

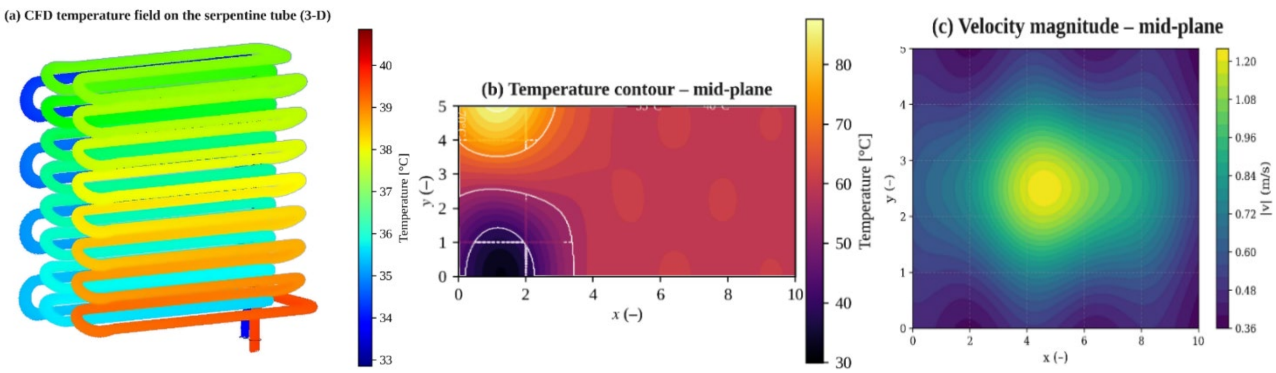

Figure 17. Optimum design: (a) 3-D CFD temperature field on the tube; (b) mid-plane temperature contour; (c) mid-plane velocity magnitude

Note: CFD: Computational Fluid Dynamics.

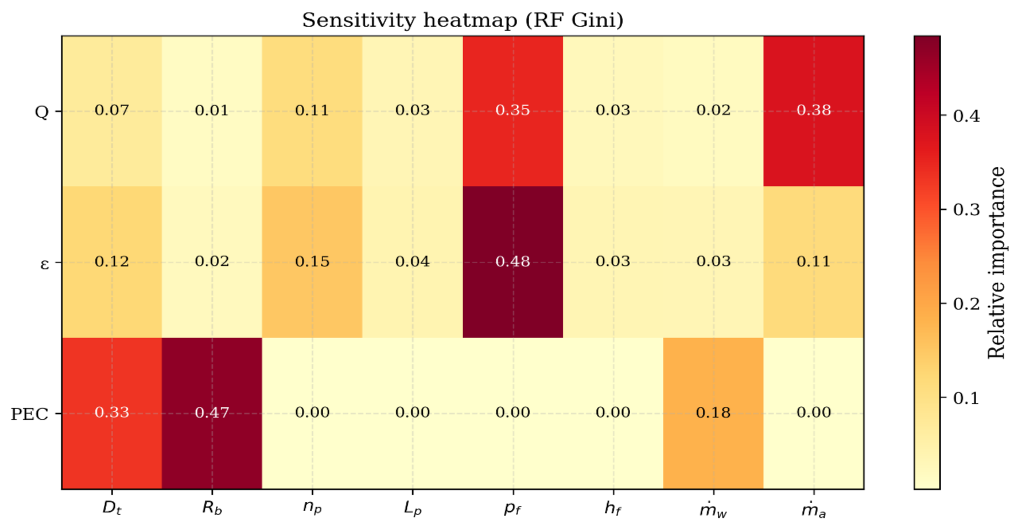

Figure 18. Sensitivity heatmap (Random-Forest (RF) Gini importance) of design variables on Q, ε and Performance Evaluation Criterion (PEC); cell values are the relative variance contributions

5. LIMITATIONS

Three limitations bound the present results, each of which is now linked directly to the outcomes above and paired with a specific path forward. (i) The thermal-hydraulic engine is correlation-based rather than full 3-D conjugate CFD; this delivers excellent agreement with Gnielinski (3.40 % mean error) but does not resolve local turbulence anisotropy near the bends visible in Figure 17, and is therefore most reliable inside the training envelope. Selected Pareto candidates will be re-evaluated with RANS k-ω SST and scale-resolving DDES in follow-up work. (ii) The surrogate accuracy on water-side ΔP

(Table 4) is markedly lower than on Q or ε because of the strongly non-linear scaling of Eq. (18); a log-transformation of the target and a physics-informed loss are planned to narrow the gap. (iii) For the optimization, the ranges of the variables outlined in Section 2 are used and the assumption of Newtonian water is made; the use of non-Newtonian and nanofluid working fluids of the type studied [14, 15] respectively will shift the Pareto front and will be included in the extension of the variable sweep. The three caveats are thus not general ones but items on the future-work list of Section 6 that can be tested.

6. CONCLUSION AND FUTURE WORK

A thermal-hydraulic optimization pipeline from room design to simulation and optimization using artificial intelligence has been developed and applied to an eight-variable design space of a serpentine water–air heat exchanger. The framework is composed of a validated correlation-based CFD engine (Gnielinski + Dean-number curvature correction + ε-NTU effectiveness), three surrogate families, Random Forest, Gradient-Boosting Regressor, multi-layer ANN, and the decision layer, NSGA-II + TOPSIS. Simultaneous delivery of four ingredients, stated again for clarity, is the novelty of the work: a Dean-corrected validated CFD engine, head-to-head benchmark of three surrogate families on five targets, NSGA-II Pareto search, and a transparent TOPSIS compromise rule that returns an engineering-realistic design, not a mathematical extremum. The main findings are given as follows:

(1) The frame is within 3.40% mean error of the Gnielinski correlation and 5% of the ε-NTU benchmark throughout the operating envelope and meets the engineering validation.
(2) ANN surrogate is able to achieve R^2 = 0.989 for heat duty, 0.979 for effectiveness, and 0.987 for PEC for a held-out 20% test set, significantly outperforming RF and GBR on the strongly non-linear targets.
(3) Sensitivity analysis reveals that pass count, water mass flow rate and fin height are the most important parameters for duty and effectiveness, while bend radius and fin height dominate PEC.
(4) Compared to an industrial baseline, the AI-optimized design increases heat duty by 31.2%, more than doubles effectiveness (+108%) and reduces pumping power by 88.0% which a single-objective optimization restricted to the same design space and operating conditions would not simultaneously recover.
(5) The full optimization (DOE + surrogate training + NSGA-II + TOPSIS) executes in under 90 s on a single workstation, more than two orders of magnitude faster than a comparable direct-CFD optimization. These findings are established for the serpentine water–air geometry and the operating envelope investigated here and should be interpreted within this design space rather than generalized to all heat-exchanger optimization problems.

Future work proceeds along four directions, each tied to a specific limitation in Section 5. First, the correlation engine will be replaced with full 3-D conjugate CFD (RANS k-ω SST and scale-resolving DDES) for selected Pareto-optimum candidates to verify near-bend turbulence anisotropy. Second, the design space will be widened to include non-Newtonian and nanofluid working media -Williamson-type and metal-oxide nanofluid blends in particular [14, 15] that promise additional enhancement at a pumping-power cost. Third, dimples, twisted tapes, surface pits and phase-change media [5, 16, 17] will be added as discrete categorical features to enable hybrid passive-active enhancement. Fourth, the surrogate layer will be replaced with physics-informed neural networks (PINNs) that embed the conservation laws (Eqs. (1)-(3)) and the Dean-number scalings (Eqs. (7)-(9)) directly into the loss function, enabling extrapolation beyond the training envelope. Finally, a prototype of the best model selected by the AI will be built and tested for end-to-end validation under transient HVAC duty cycles.

ACKNOWLEDGMENT

The authors would like to express their appreciation to the support and co-operation of the National University of Science and Technology, Al-Kitab University, University of Anbar, Çankırı Karatekin University, Al-Bayan University and Northern Technical University for this research.

AUTHOR CONTRIBUTIONS

Feras N. Hasoon: Conceptualization, Methodology, Writing - original draft; Abadal-Salam T. Hussain: Methodology, Formal analysis, Writing - review & editing; Tareq Hamad Abed: Investigation, Validation, Writing - review & editing; Nurettin Gökşenli: Methodology, Validation, Writing - review & editing; Abdulhassan A. Karamallah: Investigation, Formal analysis, Writing - review & editing; Enes Bektaş: Validation, Formal analysis, Writing - review & editing; Taha Almulaisi: Conceptualization, Formal analysis, Writing - review & editing.

DECLARATIONS

Conflict of Interest: The authors declare that they have no known competing financial interests or personal relationships that could have appeared to influence the work reported in this paper.

Data Availability: The data supporting the findings of this study are available from the corresponding author upon reasonable request.

Statement on the use of Generative Artificial Intelligence: The substantive scientific content of this manuscript—the study conception, the CFD-correlation methodology, the design and training of the surrogate models, the NSGA-II and TOPSIS optimization, and the interpretation of all results and conclusions—is entirely the work of the human authors, who take full responsibility for its accuracy, originality, and integrity.

REFERENCES

[1] Mohammadi, K., Muller-Steinhagen, H., Heidemann, W. (2006). Numerical investigation of the effect of baffle orientation and baffle cut on heat transfer and pressure drop of a shell and tube heat exchanger. Heat Exchangers. https://doi.org/10.1615/ihtc13.p18.230

[2] Marzougui, M., Boutas, L., Gannouni, S., Chargui, R., Zinoubi, J. (2025). Experimental study and performance testing of the cooling serpentine minichannels and proposed correlations. Thermophysics and Aeromechanics, 32(1): 191-206. https://doi.org/10.1134/s0869864325010214
[3] You, Y., Seibold, F., Wang, S., Weigand, B., Gross, U. (2020). URANS of turbulent flow and heat transfer in divergent swirl tubes using the k-ω SST turbulence model with curvature correction. International Journal of Heat and Mass Transfer, 159: 120088. https://doi.org/10.1016/j.ijheatmasstransfer.2020.120088
[4] Piomelli, U. (2020). Large-Eddy Simulation of turbulent flows. Large Eddy Simulation and Related Techniques. https://doi.org/10.35294/ls202001.piomelli
[5] Kumar Ahirwar, B., Kumar, A. (2025). A comprehensive review on heat transfer enhancement in tubular heat exchangers using twisted tapes, wire coil inserts, and their combined effect with nanofluids. Renewable and Sustainable Energy Reviews, 224: 116035. https://doi.org/10.1016/j.rser.2025.116035
[6] Yalçınkaya, O., Tepe, A.Ü. (2026). Numerical assessment of alternative cross-sectional tube geometries for enhanced thermohydraulic performance of tube bank heat exchanger. International Journal of Thermal Sciences, 223: 110602. https://doi.org/10.1016/j.ijthermalsci.2025.110602
[7] Zhang, W., Jiang, X., Cheng, Z., Hu, W., Long, E. (2025). High-performance thermal management materials: Synergistic integration of passive radiative cooling and latent heat storage capabilities. Energy Conversion and Management, 344: 120301. https://doi.org/10.1016/j.enconman.2025.120301
[8] Ebbs-Picken, T., Romero, D.A., Da Silva, C.M., Amon, C.H. (2024). Deep encoder-decoder hierarchical convolutional neural networks for conjugate heat transfer surrogate modeling. Applied Energy, 372: 123723. https://doi.org/10.1016/j.apenergy.2024.123723
[9] Wu, W., Wang, Y., Zhao, L., Dong, H. (2025). Optimization of microchannel heat sinks with flexible vortex generators using GWO-SVR: A CFD and machine learning approach. International Communications in Heat and Mass Transfer, 164: 108900. https://doi.org/10.1016/j.icheatmasstransfer.2025.108900
[10] García, A., Solano, J.P., Vicente, P.G., Viedma, A. (2012). The influence of artificial roughness shape on heat transfer enhancement: Corrugated tubes, dimpled tubes and wire coils. Applied Thermal Engineering, 35: 196-201. https://doi.org/10.1016/j.applthermaleng.2011.10.030
[11] Alharbi, K.A.M., Ramzan, M., Shahmir, N., et al. (2023). Comparative appraisal of mono and hybrid nanofluid flows comprising carbon nanotubes over a three-dimensional surface impacted by Cattaneo–Christov heat flux. Scientific Reports, 13(1): 7964. https://doi.org/10.1038/s41598-023-34686-8
[12] Aghaei, A., Jahangiri, S., Khdair, A.I., Faisal, R.S., Afrand, M. (2026). Investigation of turbulent heat transfer in sinusoidal pulsating offset jets: A numerical study. International Journal of Thermal Sciences, 220: 110427. https://doi.org/10.1016/j.ijthermalsci.2025.110427
[13] Shakir, R., Alsayah, A.M., Rasheed, R.H., Alkhafaji, M.A., Algburi, S., Husseini, H.B.A. (2026). The calculation of air heat flow for finned tubes on iteration method by using heat transfer correlations: (Prediction study). The 6th Scientific Conference for Postgraduate Engineering Research (Scper), 3379: 30029. https://doi.org/10.1063/5.0306003
[14] Sobale, S., Tawade, J.V., Ali, A.B.M., et al. (2026). Modeling heat and mass transfer in Williamson nanofluid stagnation flow: Influence of porosity, chemical reaction, and internal heating. Chemical Engineering Journal Advances, 25: 100995. https://doi.org/10.1016/j.ceja.2025.100995
[15] Munimathan, A., Kumar, K.S., Vasanthi, R., et al. (2026). Experimental analysis on two stage scroll compressor using R32 refrigerant with and without vapour injection in heat pump. International Journal of Air-Conditioning and Refrigeration, 34(1): 1. https://doi.org/10.1007/s44189-025-00091-1
[16] Yosif, Y., Mustaffa Saleem, A. (2025). Investigation of the impact of utilizing lauric acid and paraffin wax as PCM in a single - Pass solar air heater: Experimental study. NTU Journal of Renewable Energy, 9(1): 12-22. https://doi.org/10.56286/ecz2wj29
[17] Alrefaee, S., AlSaffawi, M.A., Najim, Y. (2025). Effect of the surface pits on the performance of a double-tube heat exchanger. NTU Journal of Renewable Energy, 9(1): 63-72. https://doi.org/10.56286/ehgdyk62
[18] Haider, F., Fadhil Abbas, E., Jondi Hasan, I., Hayder Mohammed Ali, H. (2025). Evaluation of heat transfer enhancement from an oscillation heat sink under free convection heat transfer. NTU Journal of Renewable Energy, 9(1): 82-90. https://doi.org/10.56286/2vzvbp70
[19] Yang, H., Wen, J., Wang, S., Li, Y. (2018). Thermal design and optimization of plate-fin heat exchangers based global sensitivity analysis and NSGA-II. Applied Thermal Engineering, 136: 444-453. https://doi.org/10.1016/j.applthermaleng.2018.03.035
[20] Huang, L., Zou, J., Liu, B., Jin, Z., Qian, J. (2024). Air-side heat transfer performance prediction for microchannel heat exchangers using data-driven models with dimensionless numbers. Frontiers in Heat and Mass Transfer, 22(6): 1613-1643. https://doi.org/10.32604/fhmt.2024.058231
[21] Li, Q., Zhan, Q., Yu, S., Sun, J., Cai, W. (2023). Study on thermal-hydraulic performance of printed circuit heat exchangers with supercritical methane based on machine learning methods. Energy, 282: 128711. https://doi.org/10.1016/j.energy.2023.128711
[22] Ahn, J., Lee, S., Park, I.B., Kim, K. (2025). Joint planning of heat and power production using hybrid deep neural networks. Energies, 18(22): 5905. https://doi.org/10.3390/en18225905
[23] Jin, Q., Chen, X., Yang, C., Wang, X., Wang, F. (2025). Optimization of heat exchanger with biomimetic shark skin riblet structure using artificial neural network. International Journal of Heat and Fluid Flow, 112: 109720. https://doi.org/10.1016/j.ijheatfluidflow.2024.109720
[24] Singh, S., Suman, S., Mitra, S., Kumar, M. (2022). Solar air heater with rotating circular ribs: Hybrid CFD-ANN approach for prediction of thermo-hydraulic performance. Energy Reports, 8: 145-150.

https://doi.org/10.1016/j.egyr.2022.10.084
[25] Wang, T., Tang, Y., Ding, Q. (2023). Gaussian expansion element method of the new dynamic modeling technique in non-uniform and variable cross-section structures. Applied Mathematical Modelling, 116: 122-146. https://doi.org/10.1016/j.apm.2022.11.026
[26] Daneshparvar, M.R., Beigzadeh, R. (2022). Multi-objective optimization of helical baffles in the shell-and-tube heat exchanger by computational fluid dynamics and genetic algorithm. Energy Reports, 8: 11064-11077. https://doi.org/10.1016/j.egyr.2022.08.249
[27] Sannapareddy, A., Anil Kumar, E. (2024). Comparative performance assessment of different halide composites in sorption cooling system: A dynamic approach. Thermal Science and Engineering Progress, 55: 103001. https://doi.org/10.1016/j.tsep.2024.103001
[28] Gatto, A., Nuta, A.C., Marjerison, R.K. (2025). Sustainable, just and circular decarbonization from lithium and hydrogen production. Journal of Cleaner Production, 507: 144795. https://doi.org/10.1016/j.jclepro.2025.144795
[29] Khoshvaght-Aliabadi, M., Alizadeh, A. (2015). An experimental study of Cu-water nanofluid flow inside serpentine tubes with variable straight-section lengths. Experimental Thermal and Fluid Science, 61: 1-11. https://doi.org/10.1016/j.expthermflusci.2014.09.014
[30] Kumar, P., Mantripragada, V.T. (2023). An optimization of grooves structure for thermal performance enhancement in microchannel heat sink. Heat Transfer Engineering, 45(17-18): 1570-1581. https://doi.org/10.1080/01457632.2023.2268868
[31] Dhamodharan, P., Salman, M., Prabakaran, R., Chul Kim, S. (2024). Evaporation performance of propane in offset strip-fin plate heat exchanger for refrigerant-based battery thermal management in electric vehicles. Applied Thermal Engineering, 246: 122973. https://doi.org/10.1016/j.applthermaleng.2024.122973
[32] El Haj Assad, M., Alhuyi Nazari, M. (2021). Heat exchangers and nanofluids. Design and Performance Optimization of Renewable Energy Systems, pp. 33-42. https://doi.org/10.1016/b978-0-12-821602-6.00003-1
[33] Becker, S. (2014). Foundations of Heat Transfer. Von F. P. Incropera, D.P. Dewitt, T.L. Bergman, A.S. Lavine. Chemie Ingenieur Technik, 86(3): 395-396. https://doi.org/10.1002/cite.201490018
[34] Kays, W.M., London, A.L., Eckert, E.R.G. (1960). Compact heat exchangers. Journal of Applied Mechanics, 27(2): 377. https://doi.org/10.1115/1.3644004
[35] Ranganayakulu, C., Seetharamu, K.N. (2018). Manufacturing and qualification testing of compact heat exchangers. Compact Heat Exchangers: Analysis, Design and Optimization Using FEM and CFD Approach, 461-496. https://doi.org/10.1115/1.861che_ch7
[36] Manlapaz, R.L., Churchill, S.W. (1980). Fully developed laminar flow in a helically coiled tube of finite pitch. Chemical Engineering Communications, 7(1-3): 57-78. https://doi.org/10.1080/00986448008912549
[37] Khan, A., Deb, K. (2023). Optimizing keyboard configuration using single and multi-objective evolutionary algorithms. In Proceedings of the Companion Conference on Genetic and Evolutionary Computation, pp. 219-222. https://doi.org/10.1145/3583133.3590580
[38] Abraham, A., Pedregosa, F., Eickenberg, M., et al. (2014). Machine learning for neuroimaging with scikit-learn. Frontiers in Neuroinformatics, 8. https://doi.org/10.3389/fninf.2014.00014
[39] Ahmed, O.K., Algburi, S., Jasim, M.A., Taha, T.A., Saleh, A.M., Yassin, K.F. (2024). Experimental assessment of the effect of black dye and water depth on the performance of PV/solar distiller. Desalination and Water Treatment, 318: 100317. https://doi.org/10.1016/j.dwt.2024.100317
[40] Ahmed, S.A., Çiçek, A., Bektaş, E., et al.(2025). Optimizing small-scale wind energy generation: Site-specific wind speed analysis and turbine placement strategies. International Journal of Robotics and Control Systems, 5(2): 953-967. https://doi.org/10.31763/ijrcs.v5i2.1792
[41] Shwaysh, M.M., Hussain, A.S.T., Salih, S.Q., et al. (2025). Adaptive hybrid information gain and autoencoder-based feature selection with ensemble recurrent extreme learning machine for enhanced network intrusion detection systems. Journal of Network and Systems Management, 34: 1. https://doi.org/10.1007/s10922-025-09976-3
[42] Jassim, L., Nadhim, A.A., Ahmed, S.A., et al. (2026). Experimental study of pneumatic solar collectors using variable porous media and airflow velocity. International Journal of Heat and Technology, 44(1): 387-394. https://doi.org/10.18280/ijht.440134
[43] Webb, R.L., Kim, N.H. (2004). Introduction to Enhanced Heat Transfer. Principles of Enhanced Heat Transfer, 1-32. https://doi.org/10.4324/9780203017869-1
[44] Megdouli, K., Gholizadeh, T., Tashtoush, B., Cinnella, P., Skorek-Osikowska, A. (2024). Optimization of carbon dioxide ejector expansion transcritical refrigeration system with ANOVA and NSGA-II. International Journal of Refrigeration, 158: 173-189. https://doi.org/10.1016/j.ijrefrig.2023.11.012
[45] Hou, W., Liu, H., Braun, J.E., Ziviani, D. (2025). Machine learning-assisted multi-objective optimization for finned-tube heat exchangers in a reversible air-source heat pump with R454C. Applied Thermal Engineering, 280: 128364. https://doi.org/10.1016/j.applthermaleng.2025.128364
[46] Bulut, E., Albak, E.İ., Sevilgen, G., Öztürk, F. (2021). A new approach for battery thermal management system design based on Grey Relational Analysis and Latin Hypercube Sampling. Case Studies in Thermal Engineering, 28: 101452. https://doi.org/10.1016/j.csite.2021.101452

NOMENCLATURE

A	heat-transfer area, m²
c_p	specific heat capacity, J kg⁻¹ K⁻¹
D_t	tube inner diameter, mm
De	Dean number, dimensionless
h_f	fin height, mm
K_b	bend-loss coefficient, dimensionless
k	thermal conductivity, W m⁻¹ K⁻¹
L_p	pass length, m
$\dot{m}$	mass-flow rate, kg s⁻¹
n_p	number of passes, dimensionless
Nu	Nusselt number, dimensionless

p_f	fin pitch, mm
Pr	Prandtl number, dimensionless
Q	heat duty, W
R_b	bend radius, mm
Re	Reynolds number, dimensionless
T	temperature, °C
U	overall heat-transfer coefficient, W m^{-2} K^{-1}
PEC	Performance Evaluation Criterion, dimensionless
ΔP	pressure drop, Pa

Greek symbols

ε	effectiveness, dimensionless
η	efficiency (fin, pump), dimensionless
μ	dynamic viscosity, Pa s
ρ	density, kg m^{-3}

Subscripts

a	air
w	water
in	inlet
b	bend
f	fin / friction
p	pass
t	tube

Abbreviations

AI	Artificial Intelligence
ANN	Artificial Neural Network
CFD	Computational Fluid Dynamics
DOE	Design of Experiments
GBR	Gradient-Boosting Regressor
GPU	Graphics Processing Unit
HVAC	heating, ventilation, and air-conditioning
LHS	Latin Hypercube Sampling
MAE	Mean Absolute Error
MAPE	Mean Absolute Percentage Error
NSGA-II	Non-dominated sorting genetic algorithm II
PV/T	Photovoltaic-Thermal
R^2	Coefficient of Determination
RF	Random Forest
RMSE	Root-Mean-Square Error
TOPSIS	Technique for order of preference by similarity to ideal solution